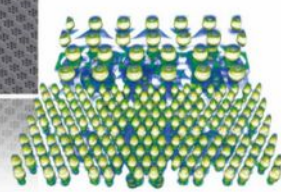




# Nanoelectronics and Its New Materials – A NEW ERA OF NANOSCIENCE

Nanoelectronics and Its New Materials –

## A NEW ERA OF NANOSCIENCE



WILEY

**Discover the recent advances in electronics research and fundamental nanoscience.**

Nanotechnology has become the driving force behind breakthroughs in engineering, materials science, physics, chemistry, and biological sciences. In this compendium, we delve into a wide range of novel applications that highlight recent advances in electronics research and fundamental nanoscience. From surface analysis and defect detection to tailored optical functionality and transparent nanowire electrodes, this eBook covers key topics that will revolutionize the future of electronics.

To get your hands on this valuable resource and unleash the power of nanotechnology, simply download the eBook now. Stay ahead of the curve and embrace the future of electronics with nanoscience as your guide.



Seeing beyond

**WILEY**

# Membranotronics: Bioinspired Nonlinear Ion Transport with Negative Differential Resistance Based on Elastomeric Membrane System

Maryam Faghih, Daniil Karnaushenko,\* Quinn A. Besford, Christian Becker, Rachappa Ravishankar, Dmitriy D. Karnaushenko, Gianaurelio Cuniberti, Andreas Fery, and Oliver G. Schmidt\*

**Biological neural networks enable rapid communication between cells, which has inspired the development of artificial smart neuro-mimetic systems. In this work, freestanding elastomeric membranes are fabricated with 3D structured holes to induce nonlinear ion-based transport. These 3D microholes are embedded in a soft polymeric membrane via a grayscale lithographical process and demonstrate ionic rectification, negative differential ionic resistance, ionic conductivity gating, and spiking under an applied electric field bias. The ion transport behavior of these membranes is affected by the shape, size, number, and chemical functionalization of the embedded microholes. The microholes are functionalized with responsive poly(*N*-isopropylacrylamide) polymer brush layers allowing to alter the electric gating behavior by external stimuli that includes temperature and chemical composition of the surrounding environment. The electrically biased membranes with a linear array of eight equidistantly spaced microholes exhibit synchronous gating of ionic transport through each one. These individual microholes are equipped with circumjacent blocking stretchable electrodes to simultaneously measure the exact onset time delay of the spikes during the synchronous gating. The operation of the freestanding elastomeric membranes with embedded microholes mimics the behavior of neural membranes. Membranotronics will pave the way toward bioinspired soft artificial neuro-mimetic systems mechanically and electrochemically comparable to their biological counterpart.**

## 1. Introduction

A biological neural membrane executes a unique functionality enabled by the characteristic electromechanical behavior of its ion transport channels. This behavior is essential for signal generation,<sup>[1]</sup> transmission,<sup>[2]</sup> and overall operation of neuronal cells<sup>[3]</sup> that has inspired the development of modern neuro-mimetic systems.<sup>[4]</sup> Among the neuro-mimetic systems, digital semiconductor-based devices offer fast signal transfer and high computational power.<sup>[5]</sup> Because of the digital nature of these circuits, they cannot well replicate the operation principle of real neurons. Therefore, there is a growing interest in building analog signal processing units relying on various electronic<sup>[6]</sup> and ionic gating and transport principles.<sup>[7]</sup> Among them, the study of ionic transport through nanopores has gained attention due to major similarities with the natural ionic channels.<sup>[8]</sup> Artificial nanopores have already shown ionic

M. Faghih, D. Karnaushenko, C. Becker, R. Ravishankar,  
D. D. Karnaushenko, O. G. Schmidt  
Institute for Integrative Nanosciences  
Leibniz IFW Dresden  
01069 Dresden, Germany  
E-mail: d.karnaushenko@ifw-dresden.de;  
oliver.schmidt@main.tu-chemnitz.de

M. Faghih, D. Karnaushenko, C. Becker, D. D. Karnaushenko,  
O. G. Schmidt  
Center for Materials  
Architectures and Integration of Nanomembranes (MAIN)  
TU Chemnitz  
09126 Chemnitz, Germany

 The ORCID identification number(s) for the author(s) of this article can be found under <https://doi.org/10.1002/adfm.202200233>.

© 2022 The Authors. Advanced Functional Materials published by Wiley-VCH GmbH. This is an open access article under the terms of the Creative Commons Attribution-NonCommercial License, which permits use, distribution and reproduction in any medium, provided the original work is properly cited and is not used for commercial purposes.

DOI: [10.1002/adfm.202200233](https://doi.org/10.1002/adfm.202200233)

Q. A. Besford, A. Fery  
Institute of Physical Chemistry and Polymer Physics  
Leibniz-Institut für Polymerforschung  
01069 Dresden, Germany  
G. Cuniberti  
Institute for Materials Science and Max Bergmann Center of Biomaterials  
TU Dresden  
01062 Dresden, Germany  
O. G. Schmidt  
Material Systems for Nanoelectronics  
TU Chemnitz  
09126 Chemnitz, Germany  
O. G. Schmidt  
Nanophysics  
Faculty of Physics  
TU Dresden  
01062 Dresden, Germany

selectivity,<sup>[9]</sup> ion current rectification (ICR) in nanoscale<sup>[10,11]</sup> as well as microscale channels,<sup>[12]</sup> non-ohmic behavior with negative differential resistance (NDR),<sup>[13]</sup> spiking,<sup>[14–16]</sup> and ionic gating properties,<sup>[17,18]</sup> that are closely replicating the behavior of biological ion channels.<sup>[8,19–22]</sup> These structures have been studied with respect to different membrane materials, pore size and shapes, and various functionalization procedures have been applied to alter the behavior of the pores.<sup>[23–25]</sup> The shape and geometry of the 3D pores, such as cones, have been inspired by the shape of biological ion channels in neuronal cells. The conical shape nanopores has been implemented in studies on ion transport through solid-state nanopores.<sup>[23,24]</sup> However, these pore systems are not easily reconfigurable and, due to their rigid and bulky structures, cannot be considered a proper artificial neuro-mimetic system, which are soft and flexible.<sup>[26–28]</sup> In this respect, flexible materials such as conducting polymers,<sup>[26]</sup> hydrogels,<sup>[29–32]</sup> planar bipolar nanofilms,<sup>[33]</sup> devices like ionic transistors and diodes,<sup>[28]</sup> liquid-metal soft-matter diodes,<sup>[34]</sup> and ion exchange membranes<sup>[35]</sup> are intriguing candidates for mimicking electrically active biological membranes. Although tunable elastomeric nanochannels<sup>[36–38]</sup> demonstrate the dynamic approach to build smart flexible nanochannel, they were not successfully mimic controlled ion transport with NDR in their system. In biological neural membranes, an action potential is generated when the depolarization voltage potential reaches a certain threshold. The generated action potential then travels along a neuronal membrane<sup>[4]</sup> as a depolarization soliton-like wave with an immediate repolarization of the membrane caused by the opening, deactivation and closing of ionic channels. This scenario is accompanied with electrical<sup>[39]</sup> processes as well as local mechanical modulations of the membrane and heat release.<sup>[40–43]</sup> To replicate the fundamental behavior of the biological neuronal membranes, new approaches need to be considered.

Here, we present an alternative strategy, which we entitle “membranotronics,” to mimic the behavior of a neuronal membrane. Membranotronics relies on nonlinear gated ionic transport across and along soft artificial elastomeric membranes influenced by an electrostatic pressure of ions across the membrane. We explore thin 7–11  $\mu\text{m}$  poly(dimethylsiloxane) (PDMS) as a base material for the elastomeric membranes. PDMS is a well-known material that can be processed with conventional photolithography-based patterning, molding technique, and etching processes.<sup>[44]</sup> The PDMS membrane is equipped with micrometer-sized asymmetric 3D transport holes. The integrated holes are designed in conical,<sup>[8]</sup> pyramidal, slope, cross, star- and slit-like shapes. Each hole in the elastomeric membrane is affected by the electrostatic pressure of the ionic charges distributed along the membrane and the hole surfaces during polarization of the membrane.<sup>[45]</sup> The PDMS membrane can be squeezed due to the excessive electrostatic pressure of ions from both sides of the membrane producing transversal strain. Due to the Poisson’s ratio nearly 0.5 of the PDMS membrane, this transversal (out of plane) strain of the thin PDMS membrane is transformed to isotropic longitudinal (in plane) strain, which leads to closure of initially opened holes. By manipulating the mechanical modulus of the membrane, the shape of the hole,

and the finding proper range of applied voltage, we can control the ion transport through the fabricated hole. The area of the hole’s cross section is inversely proportional (the theoretic background for the exact form of this dependence needs to be determined still) to the applied voltage resulting in nonlinear and NDR behavior.

This configuration enables us to acquire local and global ion-transport across the membrane at the same time. In Figure 1a–c different state of the one-hole membrane due to changes in the polarization potentials are illustrated. The electrostatic pressure of ion on both sides of the elastomeric membrane lead to compression of the membrane, variable diameter of the tip opening of the integrated hole ( $d$ ) and thickness of the membrane ( $l$ ). These continues configuration change of the membrane result in nonlinear ion transport behavior with NDR and ICR features in the current–voltage ( $I$ – $V$ ) characteristics (Figure 1d). Functionalization with poly(*N*-isopropylacrylamide) (PNIPAM) polymer brush layers causes the membranes and holes to respond to external chemical and thermal stimuli inhibiting or enhancing the transport across the membrane, that is necessary for, e.g., realizing sensing functions and communication between the membranes. It should be considered that both water and ethanol are good solvents for PNIPAM brushes, which means polymer brushes are in a swollen state in both solvents when they are pure (100% water or ethanol). The polymeric brushes are, however, in a collapsed state in a so-called critical mixture ( $\approx$ 10%–50%) of ethanol in water (co-nonsolvency effect). The hydrophilic and hydrophobic interactions in the polymer chain is the reason of this behavior.<sup>[46]</sup> PNIPAM brushes show the lowest height of polymer chain (collapsed state) at around 20% ethanol/water mixture. The height of the polymer chain is higher when the ethanol percentage is lower or higher than 20%. Therefore, in our experiment we used 20% ethanol in water to demonstrate the ion transport while the brushes are in fully collapsed state.

In the next step, we equip each of the eight integrated holes with individual circumjacent electrodes as illustrated in Figure 1e so that we are able to record the spiking behavior of the membrane globally as well as locally for each hole. Figure 1f shows the equivalent circuit of one hole. This is rather simple depiction of the solution impedance in the hole interior. However, non-trivial behavior of the charge transport within the hole is defined as a generalized impedance of the hole that includes impedance of the electric double layer and impedance of the solution inside the hole. We place the membrane with the hole between two compartments of the electrochemical cell (Figure 1g–i) filled with aqueous KCl solution of various concentrations ranging from  $1 \times 10^{-9}$  to 1 M and connected to an external source measuring unit (SMU) to apply electric bias creating electrostatic pressure across the membrane. This impedance depends on solution properties at each compartment of the electrochemical cell and bias dependent shape of the hole. We kept the bias sweep voltage always at maximum range –40 to +40 V or –20 to +20 V. Despite the big difference in solution conductivity, the charging (capacitance  $C_m$  in Figure 1f) and electrostatically driven compression of the membrane requires such high voltages to be able to squeeze the elastomeric membrane and affect the hole geometry, and as a result its impedance.

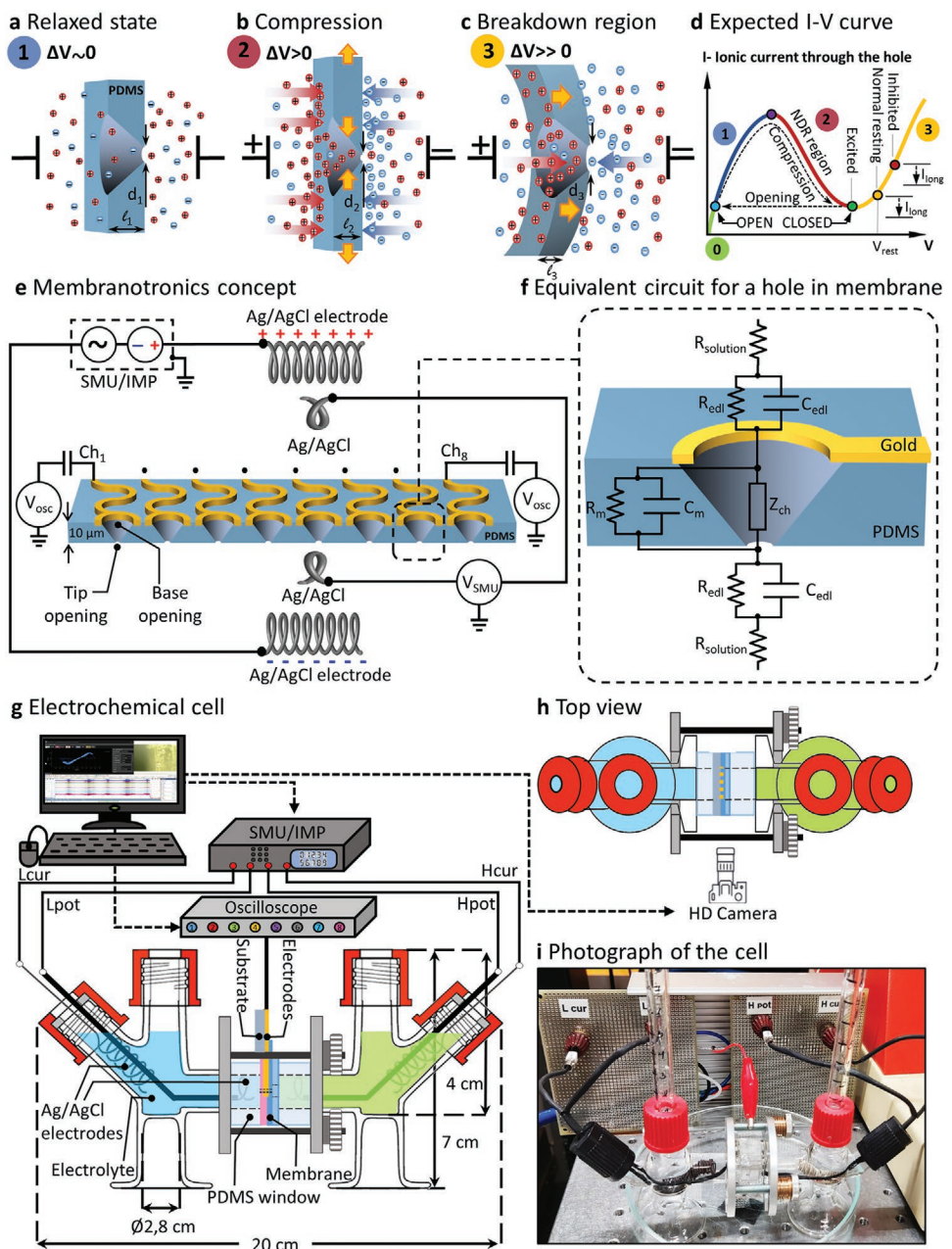


**Figure 1.** Implementation of the membranotronics concept. a) Discharged membrane (with small applied bias). b) Compression state. c) Breakdown region when the applied potential is exceeding the desired NDR threshold. d) Expected  $I$ - $V$  characteristic of a typical membranotronic unit. e) Conceptual representation of membranotronics, based on freestanding elastomeric membranes with eight blocking gold stretchable electrodes and integrated holes with electronic connections. f) Equivalent circuit for a hole in the membrane when  $R_{\text{solution}}$ ,  $R_{\text{edl}}$ , and  $R_{\text{hole}}$  are resistances of the electrolyte solution, electric double layer, and hole, respectively, and  $C_{\text{edl}}$  and  $C_m$  are the capacitance of the electrical double layer and membrane, respectively.  $Z_{\text{ch}}$  is the complex combination of impedance of the electric double layer and solution inside the hole. g) Schematic illustration of the custom-made electrochemical cell setup used for  $I$ - $V$  characterization made out of glass (10 mL each side, filled with KCl electrolyte with extra 0.01%wt. fluorescein dye on one side, with four Ag/AgCl electrodes configuration, connected to SMU/LCR). h) Top view of the electrochemical cell with camera. i) Photograph of the electrochemical setup.

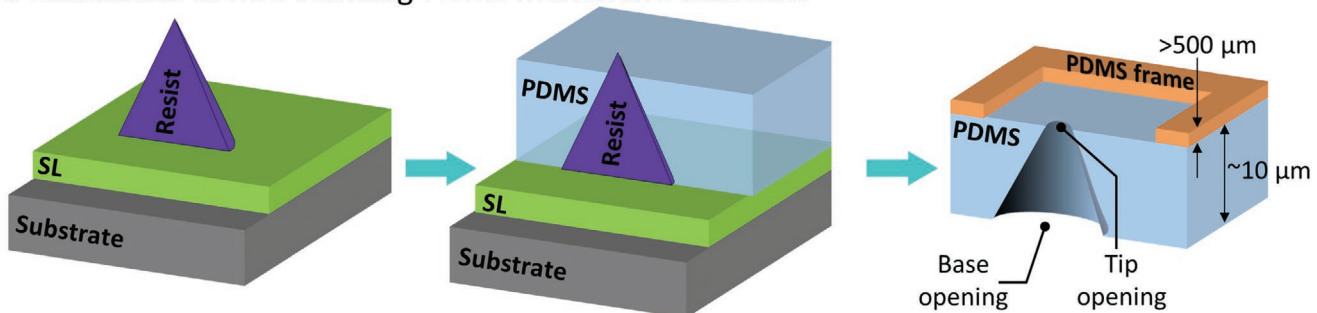
## 2. Results and Discussion

### 2.1. Freestanding PDMS Membrane Fabrication and Characterization

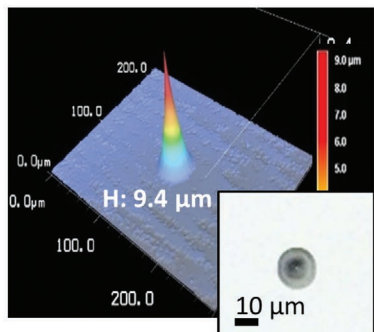
For a proof-of-concept demonstration, we fabricate the simplest membranotronic unit with a single integrated 3D shaped hole

in a thin freestanding PDMS membrane. This hole is introduced by creating a 3D structure on a sacrificial layer on a carrier glass support using grayscale lithography. The structure is then coated with diluted PDMS solution, crosslinked and delaminated from the substrate (Figure 2a, and details are in experimental section and Figure S1 and Note S2, Supporting

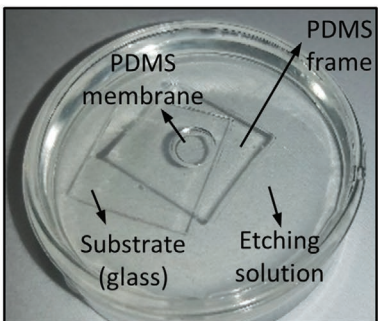
### a Fabrication of free-standing PDMS membrane with hole



### b Conical shape photoresist



### c Etching sacrificial layer



### d Free-standing membrane

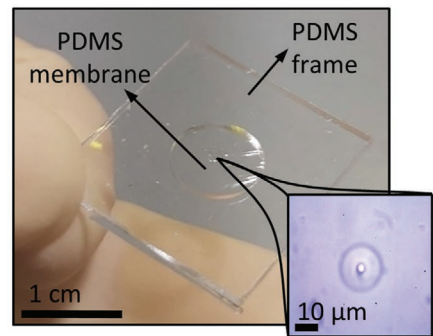


**Figure 2.** Fabrication of freestanding PDMS membrane with one integrated hole. a) Cross section illustration of PDMS membrane on conical shape photoresist and freestanding PDMS membrane after release from substrate by etching sacrificial layer and washing the photoresist (the thickness of the membrane compared to the PDMS frame is exaggerated here). b) 3D image of conical shape photoresist patterned via grayscale lithography, inset photo: top view of cone structure (images are from confocal microscope). c) Photograph of freestanding PDMS membrane after release from substrate in etching solution. d) Freestanding PDMS membrane ( $\approx 7.5 \mu\text{m}$  thickness) with integrated hole held by the PDMS frame, inset photo: optical microscope image of a conical shape hole ( $\approx 1 \mu\text{m}$  tip opening) in the freestanding PDMS membrane.

Information). We chose PDMS silicon-based elastomer material for the membrantronics project due to its low Young's modulus (2–5 MPa as shown in Figure S2a, Table S1, Note S3, and Movie S1, Supporting Information)<sup>[47,48]</sup> and perfect dielectric performance, which is necessary for electromechanical operation of the membrane (widely applied in, e.g., electronic muscles at high electric fields<sup>[49,50]</sup>). PDMS has also low ionic permeability, is chemically inert, biocompatible, optically clear, and used in micro- and stretchable electronics.

At first we prepared a lanthanum-acrylate based sacrificial layer (SL)<sup>[51,52]</sup> on a clean glass substrate followed by patterning high resolution 3D photoresist shapes via grayscale photolithography. After accomplishing the development of the resist, the desired 3D shape microstructure was observed by confocal laser scanning microscopy (Figure 2b). We have also fabricated other patterns, such as cones, pyramids, slopes, slits, crosses, and stars that can be found in Figure S3 and Table S2 (Supporting Information), and details in the Experimental Section and Note S2 (Supporting Information). The geometry of these microstructures defines the shape of the imprinted sub-micrometer sized hole in the final membrane. To fabricate the actual membrane, we optimized the concentration of the PDMS solution [pre-polymer/cross-linker 10:1 (w/w)] by mixing it with two different amounts of chloroform resulting in 50 and 25%wt. PDMS of the initial PDMS solution. By spin-coating these solutions and curing we achieved various thicknesses and elasticities of the membranes (Figure S2b,c, Supporting Information).

The PDMS solution was then spin-coated on the sharp tip end of the photoresist microstructures and cured on a hot plate. The thickness ratio between the PDMS membrane and the height of the photoresist microstructures was controlling the size of the opening at the tip of the hole in the final membrane. Unless otherwise stated, in our studies we used 7–11  $\mu\text{m}$  high photoresist 3D structures where the thickness of the PDMS membrane was chosen to be around 85% of the height of the 3D structures. A thick (several hundreds of micrometer) square-shaped PDMS frame was covalently bonded to the fully crosslinked and dry PDMS membrane providing a mechanical support to the membrane (Figure 2a right side). This frame is essential for easy handling and to prevent the membrane from crumpling due to the surface tension and hydraulic pressure of liquids during delamination and measurement. Finally, selective etching of the sacrificial layer releases the membrane with the frame into a solution as shown in Figure 2c. The floated membrane still contains the photoresist structure that blocks the hole and by applying an appropriate solvent this photoresist structure is dissolved leaving the open hole in the free-standing PDMS membrane (Figure 2d). The exact characterization of the final freestanding membranes with SEM and FIB did not give clear images due to the strong charging of the membranes even with deposited conducting layers. Therefore, we can only refer to optical images in this study. In future investigation of such membranes, performing X-ray imaging with a contrast enhancing additive to better assess the geometry of the final

membrane could be a possibility for imaging the created hole in membrane.

The *I*-*V* curve of the fabricated membrane was measured in a custom designed electrochemical cell made out of glass with two identical compartments. The fabricated membrane is pressed in-between two flanges with optically clear PDMS gaskets also serving as a window for observing the membrane with a microscope camera. The cell is equipped with four inhouse-made silver chloride (Ag/AgCl) electrodes. The cell is filled with the desired concentration and amount of KCl electrolyte solution ( $1 \times 10^{-9}$ –1 M) on each side of the cell under ambient conditions allowing chemical gradients to be induced as well as the hydrostatic pressure across the membrane (Figure 1g–i and Figure S4 and Note S1, Supporting Information). We altered the concentration of the solution allowing to tune the impedance and affect NDR and ICR properties of the holes. We added fluorescein to the electrolyte on one side of the cell to be able to observe the fluid stream gated when varying the biasing voltage across the membrane. Once the direct current (DC) bias voltage is applied, an electrostatic field builds up across the membrane.

This electric field induced pressure that compresses the elastomeric membrane mechanically. The mechanical properties of the elastomer as well as the geometry of the integrated hole leads to various operation regimes depending on the biasing voltage (Figure 3a,b). We performed multiple scans from +20 to -20 V revealing nonlinear *I*-*V* curves of the PDMS membrane with one integrated hole showing very good stability. In the first area (Figure 3a-I,b) the membrane is in a noncompressed state (low electric potential across the membrane) and the ionic current flows through the hole with almost linear ohmic behavior with a nonlinear variation of the current at high biasing potentials. In the second area (Figure 3a-II,b) the ionic current flow changes nonlinearly with the biasing current and the ionic current saturates reaching its maximum at higher biasing potentials.

This mode of operation also leads to an observable stream of liquid from one compartment to the other. In the higher voltage side of this area, the exerted electrostatic pressure on the surface of the membrane starts to mechanically squeeze the elastomeric membrane and reduce the hole opening at its tip. In the third area (Figure 3a-III,b) the ionic flow shows an NDR character leading to the reduction of the flow and disappearance of the stream due to narrowed hole opening. This leads to the nonlinear behavior in the *I*-*V* curve possessing the NDR with an almost complete current blocking through the hole. With the biasing voltage is in area II and III the ionic current through the hole leads to nonlinear oscillations of the current through the membrane (Figure 3b,c). Once the applied potential is reduced, the membrane depolarizes and comes back to its original state (Movie S2 and Sound S1, Supporting Information). We confirm this behavior by applying hydrostatic pressure across the membrane where for different pressures the hole opening is different and, in this way, the NDR behavior is enabled or disabled (Figure S5 and Note S4, Supporting Information) The effect of the electrostatic compression on the membrane was also confirmed by the electrical impedance measurement of the membrane under various biases (Figure S6 and Note S1, Supporting Information).

We also fabricated freestanding PDMS membranes with one hole but with different geometries of the hole for all global ion-

transport studies. In Figure 3d, nine different 3D photoresist structures in six different base diameters (ranging from 50 to 800  $\mu\text{m}$ ) were patterned and characterized. We demonstrate that nonlinear *I*-*V* behavior can be achieved by optimizing size and shape of the single hole integrated within the elastomeric membrane (Figure 3d–g). Figure 3e shows *I*-*V* curves of an as-fabricated closed membrane which could be due to an improper shape or size of the 3D structure. Figure 3f,g demonstrates a typical behavior of the correctly operating membrane with NDR behavior. As can be seen in Figure 3f, the ionic transport performance is nearly unchanged after 100 cycles of applied electric field across the membrane. Figure 3h shows linear *I*-*V* curves because the membrane has a crack or the integrated hole has a big tip opening. Based on these experiments, the NDR phenomenon observed here is reproducible for a distinct hole shape and size combination. For instance, conical shape #3 is the most robust and versatile shape among all the designs for producing membranes possessing reproducible nonlinear behavior in the global ion-transport measurements, for the widest range of the dimensions demonstrating the long-term performance. Therefore, only this design was used for further local ion-transport studies with integrated microelectrodes. While the slit design (design #6 in Figure 3d) has shown the lowest NDR onset voltage, narrowest operating range of base diameters and the very sharp NDR response suggesting high sensitivity to changes in geometry of the hole (Figure 3g). This design has been used for functionalizing the membrane with PNIPAM brushes.

We studied the behavior of the conical hole in presence of the concentration gradient (Figure 3i,j). In these experiments, we filled both sides of the membrane (conical shape #3 in Figure 3d) with different concentrations of KCl electrolyte ( $1 \times 10^{-9}$  M vs  $1 \times 10^{-3}$  M) and observed a clear ICR.<sup>[23,53]</sup> Diffusion of ions from high concentration side to low concentration side prevents the membrane from oscillations at  $\pm 40$  V. Thus, in Figure 3i we increased the voltage range twice until the possible hardware limit to test the NDR response, which we have not observed, despite the presence of ICR. The ICR occurs due to charge accumulation and depletion of ions on the wall surface and inside of the hole.<sup>[23]</sup> It is known that ionic current rectification can also be achieved in microscale channels with the concentration gradient across the channel<sup>[12,54,55]</sup> and a surface charge, such as it has been observed in our work. The concentration values for nanochannels are usually in the range of  $\text{mM L}^{-1}$  values that can be projected to 1–10 nm Debye screening length (effectively the diffusion layer thickness), comparable with the nanopore size. In our work we apply much lower concentration  $1 \times 10^{-9}$  M  $\text{L}^{-1}$  of the solution on one side with the Debye screening length of around 10  $\mu\text{m}$  (Figure S7 and Note S5, Supporting Information). This value is comparable to the scale of our holes. We have observed ion rectification depending only on the sign of the ion concentration gradient, the hole shape had no direct influence on the rectification behavior. Based on several reproducible experiments we expect that the rectification in our system solely depends on the direction of saline gradient caused by diffusion through the hole and independent on the shape of the hole.<sup>[54]</sup> Modulation of the electric double layer (effectively the diffusion layer) happens due to change in concentration of ions inside the channel,

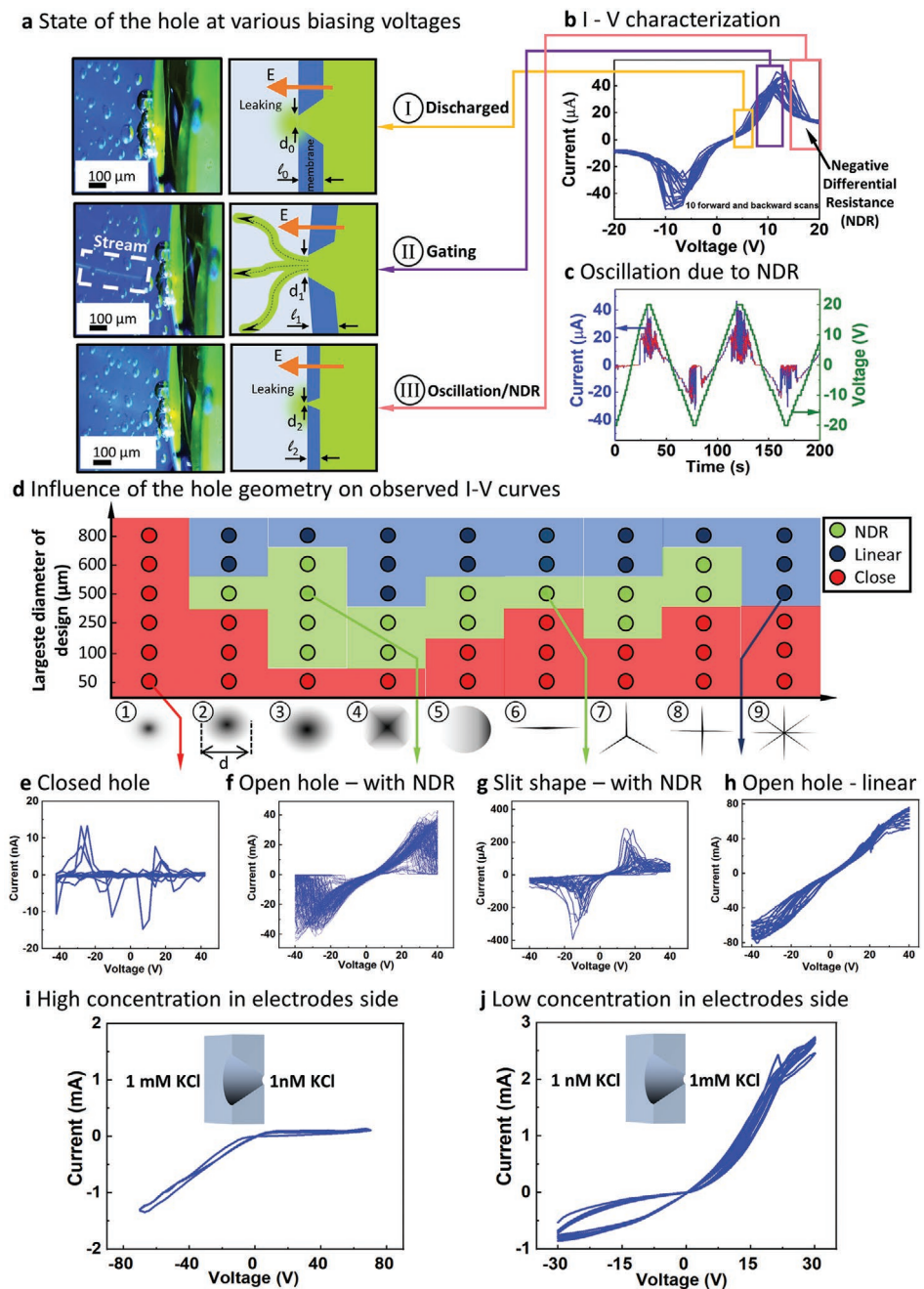


**Figure 3.** Implementation of the membranotronics concept. a) Different state of the hole during biasing voltages: Ionic conductivity changes across the membrane while changing external electric bias which leads to ionic current at low potential and closure of the hole at higher potential ( $l_0 > l_1 > l_2$  and  $d_1 > d_0 > d_2$ ). b) I-V characteristic of the PDMS membrane with one hole while voltage was sweeping between  $\pm 20$  V, clearly observing the NDR region. c) Nonlinear oscillations of the current through the membrane due to NDR. d) Qualitative illustration of the influence of the hole shape and size on ionic transport in I-V curves based on nine different shapes and six different sizes of the integrated hole in the PDMS membrane. Membrane thickness in all the samples is provided with respect to height of the 3D photoresist structures (around 85% of photoresist height) and voltage was sweeping between  $\pm 40$  V. e) Typical I-V curve observed for closed membrane (ten forward-backward cycles). f) 100 cycle stability study of membrane with NDR feature and nonlinear oscillations of the current through the membrane. g) I-V curve of membrane with slit shape design possessing NDR (ten forward-backward cycles). h) Linear I-V curve due to the large integrated hole in membrane or broken membrane (ten forward-backward cycles). i) Rectified I-V curve in presence of concentration gradients across the PDMS membrane (10  $\mu\text{m}$  thickness) with conical integrated hole ( $d = 600 \mu\text{m}$ ). j) I-V curve when electrolyte with lower concentration is located at base opening side of the hole.

which is described in ref. [55]. We also depict the behavior of the electric double layer (effectively the diffusion layer) in Figure S8 (Supporting Information). We believe that high current and

high voltage rectification in microhole sized membranes may find application in such fields as saline gradient driven power generation.<sup>[56,57]</sup>

## 2.2. Functionalization of the Membrane

We functionalized the surface and inner wall of the hole (**Figure 4a,f**) with PNIPAM polymer brush layers to investigate stimuli-driven blocking or closing of the holes due to the conformation of the PNIPAM under different environmental conditions. Integrating PNIPAM brushes into our system allows for an orthogonal chemical or thermal stimulus that can operate in parallel with electrical response of the membrane. Addition of this feature into these systems is important to modulate the electric behavior of the membrane similar to that of the neuronal synapses and sensory system of living cells that alter the response of the neural system. This functionalization of the membrane enables a direct interaction of the membrane with the external surrounding environment.<sup>[58,59]</sup> The thermosensitive PNIPAM brushes serve as a layer that can change its phase from a swollen state to a collapsed state and vice versa in response to environmental stimuli<sup>[60]</sup> and, as a result, change the ionic permeability of the hole. Furthermore, the PNIPAM brushes anchored to the soft PDMS surface have the ability to actuate or bend the PDMS as a function of conformation,<sup>[61]</sup> meaning this could lead to selective closure of the pore, if the geometry permits it. **Figure 4b,g** shows the operational principle of the functionalized hole in the elastomeric membrane where the walls and surrounding surface of the hole were covered with PNIPAM brushes that can be activated by temperature<sup>[62,63]</sup> or stimulated by exploring so-called co-nonsolvency<sup>[46]</sup> effects (i.e., a mixture of two good solvents causes the collapse or demixing for the polymer). More details on the functionalization and the operation principle can be found in Figures S9 and S10 and Note S6 (Supporting Information). The impact of PNIPAM brushes on the ion conductance through the hole was demonstrated through a sharp phase transition of the PNIPAM brushes in water at the lower critical solution temperature (LCST) of 32 °C, and at co-nonsolvency conditions (e.g., 20% vol. ethanol in water mixture). The PNIPAM brush layers were grafted to (3-aminopropyl triethoxysilane (APTES)<sup>[59]</sup>-modified PDMS membranes by 4-(4,6-dimethoxy-1,3,5-triazin-2-yl)-4-methyl-morpholinium chloride (DMTMM) catalyzed amide coupling to carboxylate end-group PNIPAM. For this part of the study only the slit shaped structures (structure #6 in **Figure 3d**) were used to create holes in the PDMS membrane. This shape was chosen as the swollen PNIPAM brush layers were anticipated to have a swollen thickness of about 100 nm based on previous PNIPAM brushes of similar  $M_N$  (average molecular weight) PNIPAM,<sup>[64]</sup> therefore requiring a very narrow hole opening. Using the slit shaped structures create a crack with a narrow opening in the final freestanding membrane, which has the potential to be closed by the force of the collapsing/swelling polymer brush. This makes it possible for the PNIPAM brushes to have an effect on ion transport in their collapsed or swollen state. We believe that the reason behind this is the high sensitivity of the slit shape of the hole to changes in the slit geometry with the stretching and collapsing PNIPAM brushes with environmental stimuli, whereby the extending polymer brushes both create a blockage in the channel, as well as driving a force towards slit closure as the chains repel away from the anchoring surface. Others have shown that PNIPAM brushes immobilized on thin

PDMS materials have the ability to reversibly bend the material in response to changing polymer conformation. The following experiments were performed in the same electrochemical cell with 1 M KCl electrolyte concentration on both sides of the cell. The final two freestanding PDMS membranes were equipped with one integrated slit shaped hole with a base size of 50 μm × 2.5 μm and 500 μm × 6 μm (**Figure 4a,f**). The effect of the LCST on the ion transport of the membrane was recorded in time with small applied bias (0.1 V) (**Figure 4c**) showing clear ion current gating through the membrane when the brushes were collapsed or swollen at different temperatures. In another experiment we swept the bias from -40 to +40 V (**Figure 4d**) when changing the temperature of the electrolyte, which revealed a clear change in the ionic conductance through the hole for the two brush states. As can be seen in **Figure 4e**, the ionic current across the membrane was reduced to about 10% of the original value at room temperature, where the PNIPAM typically reduces to ≈25% of its fully swollen thickness above the LCST.<sup>[64]</sup> The control measurement for this experiment on a similar membrane without integrated PNIPAM brushes can be found in **Figure S11** (Supporting Information).

Changing the electrolyte consisting of 20% vol. ethanol (EtOH) in 1 M KCl also significantly affected the ionic current passing through the hole of the functionalized membrane (**Figure 4h**), which is the point of the co-nonsolvency-induced collapse of the PNIPAM brushes.<sup>[46]</sup> In the collapsed state, we observed substantially increased nonlinearity in the I-V (**Figure 4h,i**) curves when compared to the swollen state. This result is consistent with the co-nonsolvency-induced transitions of the PNIPAM chains from one state to the other, which influences ionic transport through the membrane at different biases (electrostatic compression states). Previous studies have used similar concepts to control the translocation of DNA through PNIPAM-decorated nanopores.<sup>[65]</sup>

## 2.3. Local Potential Measurement around the Holes

A second type of freestanding PDMS membrane was designed and fabricated to study the local ion-transport properties of the membrane near the hole. These samples were designed to have 1, 2, 3, or 8 holes. For this purpose, two layers of polyimide (PI) and stretchable electrodes were added to the membrane system (**Figure 5a**). The PI layer was fabricated using conventional photolithography and Ø360 μm holes were dry-etched with O<sub>2</sub> plasma. The PI layer was added to increase the mechanical stability of stretchable electrodes and in addition to serve as an insulation layer between the backside of the electrodes and the electrolyte. Afterwards, a lift-off method was used to create eight stretchable electrodes<sup>[66]</sup> with a serpentine design out of Cr<sup>5</sup> nm/Au<sup>50</sup> nm.

For the electrode-integrated samples, only the conical shape photoresist with 600 μm base diameter was used on top of the electrodes (**Figures S12 and S13**, Supporting Information, and further details are discussed in Note S2, Supporting Information). The realization of the PDMS membrane, etching of the sacrificial layer, and washing away the photoresist were similar to the other membranes. For these samples a flexible cable was bonded and sealed on each sample and then connected to

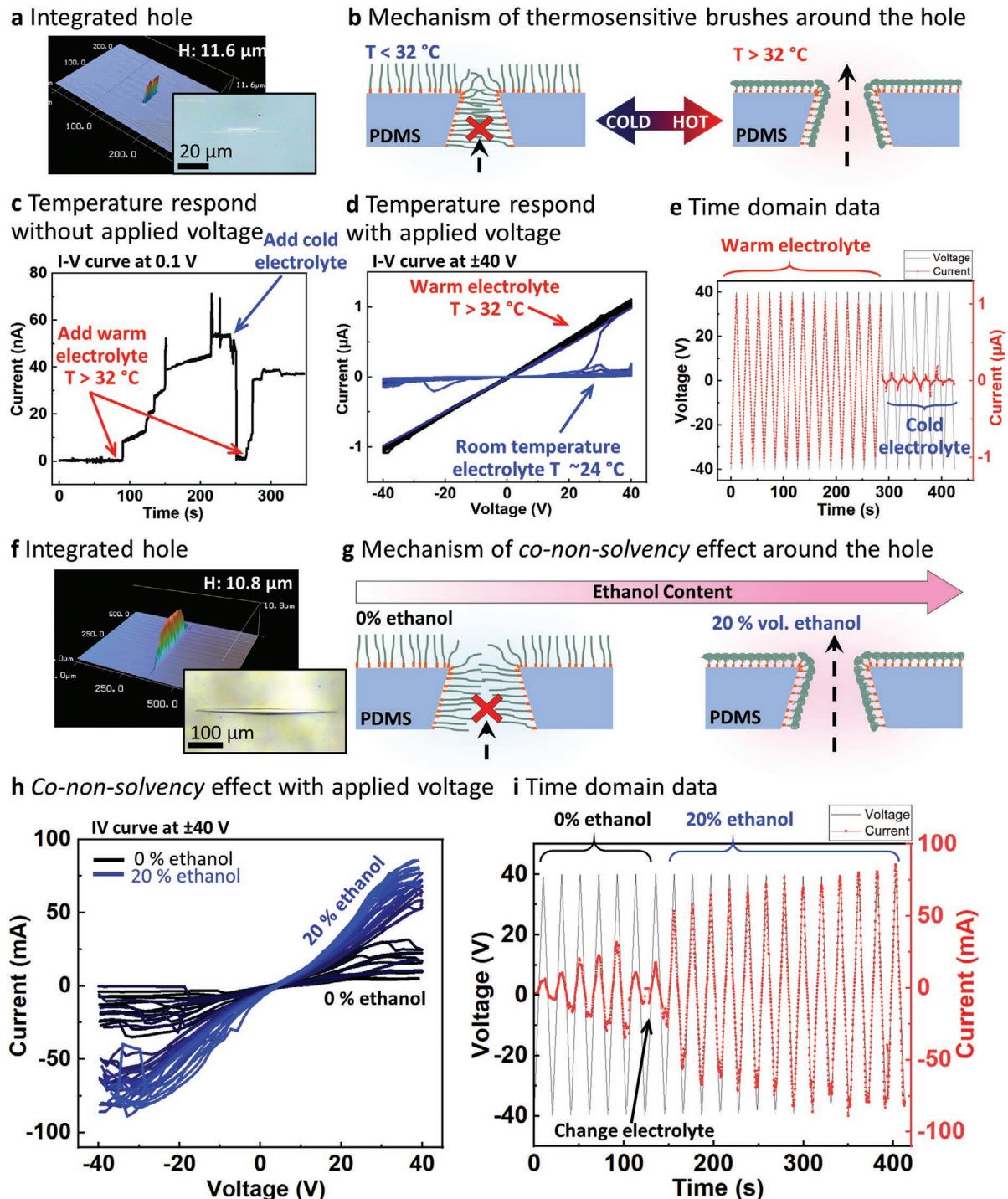
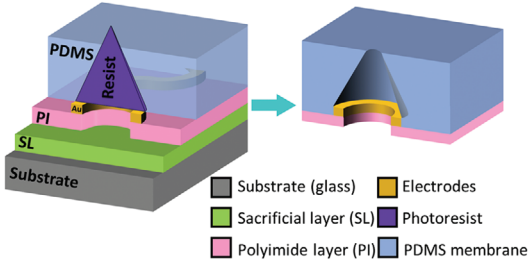
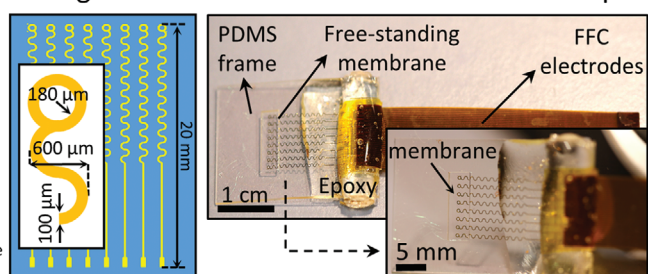


**Figure 4.** Temperature response and co-nonsolvency effect of PNIPAM brush layers. a) 3D profile of the slit shape photoresist with confocal microscope ( $d = 50 \mu\text{m}$ ,  $H = 11.6 \mu\text{m}$ ) and optical microscope images of the integrated hole in a  $10 \mu\text{m}$  thick membrane. b) Proposed mechanism for the PNIPAM brushes around the hole of freestanding PDMS membrane at different temperatures. At a temperature below the lower critical solution temperature (LCST:  $32^\circ\text{C}$ ), stretched PNIPAM brushes close the hole. At temperatures higher than  $32^\circ\text{C}$ , PNIPAM brushes collapse and open the hole. c) Current response for freestanding PDMS membrane grafted with PNIPAM brushes inside the electrochemical cell with small applied bias ( $0.1 \text{ V}$ , electrolyte:  $1 \text{ M KCl}$ ) when changing electrolyte with different temperature. d) I-V curve of same membrane during biasing ( $\pm 40 \text{ V}$ , 20 forward-backward cycles) and changing electrolyte ( $1 \text{ M KCl}$ ) with different temperature. e) Time domain data of measurement on panel (d). f) 3D profile of the slit shape photoresist with confocal microscope ( $d = 500 \mu\text{m}$ ,  $H = 10.8 \mu\text{m}$ ) and optical microscope images of the integrated hole in the  $9 \mu\text{m}$  thick membrane. g) Proposed mechanism for co-nonsolvency transition of the PNIPAM brushes around the hole of freestanding PDMS membrane in pure water versus 20% vol. ethanol in water. h) I-V curve of PDMS membrane grafted with PNIPAM brushes inside electrochemical cell while biasing the voltage ( $\pm 40 \text{ V}$ ) and changing electrolyte. Black lines are  $1 \text{ M KCl}$  in DI water and blue lines are 20% vol. ethanol in  $1 \text{ M KCl}$  in DI water. i) Time domain data of measurement on panel (h).

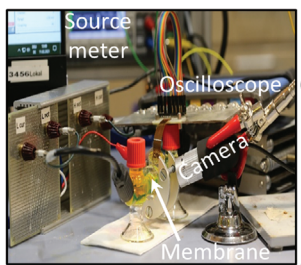
**a Membrane with embedded electrode**



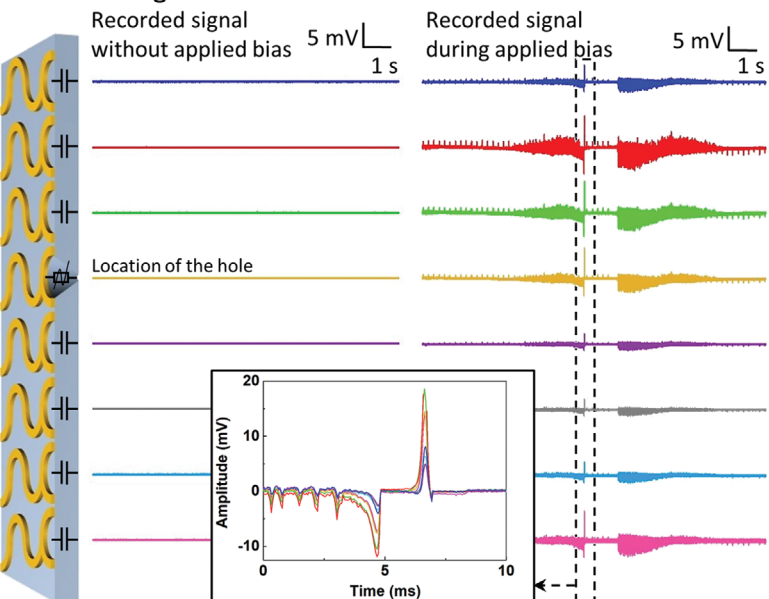
**b Design of stretchable electrodes and final sample**



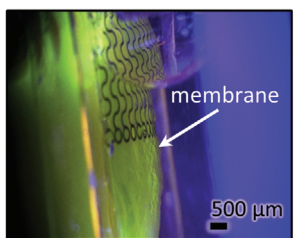
**c Photograph of the set-up**



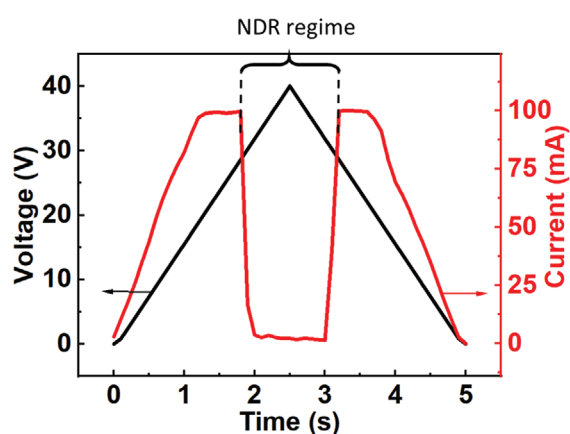
**e Recorded signal for a membrane with one hole**



**d Membrane in the cell**



**f Time domain data**



**g Discharging propagation for 8 holes membrane**

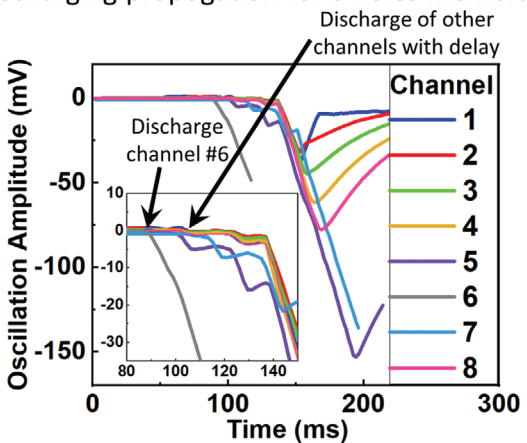


**Figure 5.** Characterization of freestanding membrane with stretchable electrodes and integrated holes. a) Cross section illustration of PDMS membrane on conical shape photoresist and stretchable electrode and freestanding PDMS membrane after release from substrate by etching sacrificial layer and washing the photoresist (the thicknesses are exaggerated here). b) Left panel: Design of eight stretchable electrodes and details of the Serpentine design of one stretchable electrode. Right panel: Photograph of final free-standing membrane with bonded FFC cable. c) Photograph of setup during measurement with oscilloscope. d) Photograph of PDMS membrane with stretchable electrodes inside the electrochemical cell. e) Recorded signal via oscilloscope for a membrane with one hole (10 μm thickness) in 1 M KCl on both sides of the cell; left graph: control experiment without applied bias, right graph: during applied bias (scale bars: 1 s, 5 mV for both measurements). Inset shows magnification of start of the oscillation. f) Time domain data for data in panel (e) with applied bias. g) Discharging channel #6 during saturation time for a PDMS membrane with eight holes revealing the propagation of discharging signal first with neighboring channels (in light blue and purple colors) and rest of channels (this data was acquired with a concentration gradient of  $1 \times 10^{-9}$  M versus 1 M KCl). One can observe 12.6 ms delay between channel #5 and #7. There is no observable delay among other channels, probably because the working point of these holes is not at NDR area of operation.

an oscilloscope with eight simultaneously sampling channels (Figure 5b).

The propagation of a solitonic pulse/wave along the neuronal membrane surface when experiencing an action potential has already been reported.<sup>[41,67]</sup> We expect a similar to natural neural membrane electrochemical signal propagation behavior along the fabricated membrane with holes. We also believe that the presented system behaves similar to, e.g., an electrical parametric nonlinear transmission line<sup>[68,69]</sup> which requires a precise tuning of transmission line parameters to allow a soliton like pulse propagation along the line. For this experiment, free-standing PDMS membranes with 1, 2, 3, and 8 conically shaped holes and integrated stretchable electrodes near each hole were fabricated (Note S2, Supporting Information). Electrodes in the close vicinity to the holes are required to detect the signal propagation process along the membrane surface and locally characterize the behavior of the membrane around each hole. The stretchable electrodes were connected to a flat flexible cable (FFC) which was fed outside of the electrochemical cell at one side. The FFC was connected to eight channels high-precision oscilloscope with a sampling rate of 1–20 MHz at the other side enabling simultaneous sampling of all channels during measurement (Figure 5c,d). This configuration enables us to simultaneously monitor local and global ion-transport across the membrane. Note S1 (Supporting Information) provides more detailed information about this measurement.

We recorded signals for a membrane with one hole, without and with applied bias as shown in Figure 5e. By applying bias voltage from 0 to +40 V all eight channels of the membrane showed oscillations. As can be seen from Figure 5e, all of the eight electrodes picked-up spikes/oscillations at the same time, without any time delay due to simple capacitive coupling through the electrolyte (Figure 5e inserted graph). When a high potential was applied across the membrane, creating high electrostatic pressure on the membrane, the hole closed (between +30 to +40 V and vice versa) stopping the membrane from oscillating (NDR regime). All eight channels showed this response. This data agree with the time domain data acquired from the global ion transport in the electrochemical cell during the measurement shown in Figure 5f. The ionic current drops to almost zero during the NDR regime and the recorded signal showed no oscillation for all the channels.

Next, we characterized the membrane with eight conically shaped holes. We applied sufficiently high potential across the membrane to keep the membrane in the critical/oscillating regime. Then, the membrane was discharged/depolarized at a specific time point by applying an external potential pulse to electrode #6. The recorded signal in Figure 5g shows a clear delay between the spike of this channel and the neighboring channels (14.4–50.4 ms). This result has been confirmed for the two-hole membrane as well (Figure S14, Supporting Information).

This recorded delay during the depolarization shows that the electrochemical signal can propagate along the active membrane, similar to a distributed nonlinear transmission line (parametric amplifier).<sup>[70–72]</sup> The membranotronics rely on nonlinear and NDR regions of the holes integrated into the membrane allowing to generate and transmit pulses along the surface by cycling between its compressed resting state and

uncompressed ion conducting state. This signal is an electrochemical/mechanical propagation of the ionic current. To preserve the shape of the pulse over a prolonged distance along the membrane all of the holes should be set to a correct working point around NDR region by a proper design and electrical bias. For instance, the value of the bias voltage required for closing the microhole and reaching the NDR regime should reduce with decreasing the size of electrochemical cell, reducing Young's modulus of membrane material, its thickness, and size of the hole opening. These parameters have to be considered and fine-tuned for further development of membranotronics systems to achieve the generation and propagation of electro-mechanical pulses along the membrane.

### 3. Conclusions

In conclusion, we have demonstrated a novel strategy, namely, the membranotronics, bioinspired by mechanical and electrochemical properties of biological neuronal membranes based on artificial elastomeric membrane system with integrated holes. The electrochemical and mechanical properties of the fabricated membranes were investigated through global and local ion transport studies of membranes. An environmental response for this new system has been observed with functionalized PNIPAM polymer brush layers. We demonstrated that the grafting of functional polymers onto our membrane can affect the ion-transport behavior of the membrane in response to environmental stimuli such as temperature and electrolyte content, consistent with known phase transitions of PNIPAM, which opens up intriguing ways to mimic neuronal synapses. The elastomer membrane with integrated holes demonstrates NDR, ion current oscillation, ICR, and propagation of an ionic pulse along the membrane surface enabling more complex membrane based artificial neuromimetic systems. Demonstration of some application scenarios relying on the described mechanisms is an important goal of this multistage work. For instance, it would be intriguing to tune the parameters of the membranotronic system to achieve stable generation and propagation of a solitonic pulse as it has been theoretically predicted for some electrical nonlinear transmission lines to mimic behavior of, e.g., axons, synapses, and implement sensing functions. We believe that high current and high voltage rectification in microhole-sized membranes may find application in such fields as saline gradient driven power generation. However, this work is still at its proof of concept stage requiring more elaborated future development that should include modeling and theoretical investigation of the system, finding critical system parameters such as solution concentrations, geometries of holes, bias potential, membrane elastic properties, and its thickness to name a few. We believe that membranotronics will take us one step closer to mimic biological neuronal membranes, which could be a key element toward artificial intelligent systems, soft robotics, and bioinspired electronics. Even though the main goal of membranotronics is to biomimic biological neuronal system, the proposed method of elastomer membrane can be adapted accordingly into different fields of life sciences and materials sciences.

## 4. Experimental Section

**Preparation of Substrates and Materials:** Float glasses with  $100 \times 100 \text{ mm}^2$  and 1 mm thickness were used as substrate (D263T eco glass, SCHOTT AG, Mainz, Germany) in this study. A professional washer PG85 (Miele & Cie. KG, Gütersloh, Germany) was used to wash the substrates followed by the surface activation with oxygen plasma in the GIGAbatch 310M (PVA Metrology & Plasma Solutions GmbH, Wettberg, Germany) and surface functionalization with a monolayer of 3-(trimethoxysilyl) propyl methacrylate (TMSPM) (VWR, Darmstadt, Germany) in a vacuum oven at  $150^\circ\text{C}$  for 2 h under weak vacuum. SL and PI were synthesized following previously reported procedures.<sup>[51,52]</sup>

**Fabrication of Freestanding PDMS Membrane:** SL was spin-coated at 1000 rpm for 60 s and photopatterned on functionalized glasses to form a thin layer ( $\approx 200 \text{ nm}$ ). Then diluted PI layer was spin-coated on top of SL at 2000 rpm for 60 s and backed at  $220^\circ\text{C}$  for 10 min under nitrogen atmosphere to form an  $\approx 500 \text{ nm}$  continues layer. To create a hole for passage of electrolyte through the membrane, 1 or 2 or 3 or 8 hole(s) (360  $\mu\text{m}$  diameter each) was/were created on the PI layer respect to the placement of electrode ring. Holes in the PI were patterned via standard lithography (AZ5214E Microchemicals GmbH, Ulm, Germany) and etched by  $\text{O}_2$  plasma in reactive ion etching (RIE) (Plasma Lab 100; Oxford Instruments PLC, Abingdon, UK). Eight stretchable electrodes with Serpentine design were patterned on structured PI through a standard lift-off process. The conductive electrode layer consists of  $\text{Cr}^{5 \text{ nm}}/\text{Au}^{50 \text{ nm}}$  were deposited using e-beam evaporator (Plassey MEB 550S Electron Beam Evaporator) (base pressure:  $1 \times 10^{-6} \text{ mbar}$ ; deposition rate:  $4 \text{ \AA s}^{-1}$ ). Subsequently, sample was soaked in acetone for 30 min to lifting off the underlying photoresist layer and rinsed with isopropyl alcohol. (For membranes without electrodes PI layer and electrode layer was not deposited.) At this point each sample was diced in to  $30 \times 30 \text{ mm}^2$  as a size of single device. Different shape and size of 3D structures were designed using CorelDRAW X8 software. First each sample was spin-coated with a positive photoresist (AZ4562 Microchemicals GmbH, Ulm, Germany) at 1000 rpm for 60 s and prebaked at  $100^\circ\text{C}$  for 2 min and patterned via grayscale lithography by a maskless aligner (MLA 100, Heidelberg Instruments Mikrotechnik GmbH, Heidelberg, Germany) at  $700 \text{ mJ cm}^{-2}$ . Finally developed with AZ826 MIF developer (Microchemicals GmbH, Ulm, Germany) solution for around 7 min and rinsed with DI water. Development time was slightly different for each sample based on the design of 3D structures. Laser scanning confocal microscope (VK-X210, Keyence Deutschland GmbH, Neu-Isenburg, Germany) and DekTak Stylus profilometer (Bruker, Billerica, MA) were used to measure the height of each design. 25%wt. PDMS solution in chloroform was spin coated on each sample with respect to height of photoresist structure(s) and backed for 12 h on a  $90^\circ\text{C}$  hot plate. The thickness of membrane for all the samples was around 85% of the 3D structure photoresists height. Next, each sample was bonded to a flat flexible cable (FFC) and encapsulated with a thin epoxy resin (HP-E5K, HP-Textiles GmbH, Germany) from both sides. To ease the handling of the freestanding membrane, 2 mm thick PDMS frame with  $10 \times 3 \text{ mm}$  rectangular shape open window in the middle was bonded on top of the PDMS membrane using oxygen plasma (Diener Femto, Diener electronic, Ebhausen, Germany) with 35 SCCM  $\text{O}_2$ , 50 W for 30 s and covalently bonding on  $120^\circ\text{C}$  hotplate for 5 min with applied manual pressure. Finally, SL was selectively etched in 1:4:100 (vol.) mixture of perchloric acid 70% (PanReac Quimica S.L.U., Barcelona, Spain): hypophosphorous acid 50% (Fisher Scientific, UK): DI water solution at room temperature for  $\approx 48$  h and photoresist was washed away in acetone. (Details on the membrane fabrication are provided in Note S2, Supporting Information.)

**Electrochemical Characterization of Fabricated Membrane:** A custom made glass electrochemical cell (Forschungszentrum Jülich, Jülich, Germany) consists of two compartments with equal volume (10 mL) was used for electrochemical measurements. The cell was performed in four-electrode configuration made out of Ag/AgCl. The fabricated freestanding membrane was assembled between two house-made PDMS windows and fixed by an aluminum flange. Prior to each measurement,

each compartment of the cell was filled with desired concentration of KCl (Sigma-Aldrich Co. LLC., Germany) in DI water. Semiconductor grade ultrapure water was used from the clean room purification system for the experiments (resistivity better than  $16 \text{ M}\Omega \text{ cm}$ ). The  $1 \times 10^{-9} \text{ M}$ ,  $1 \times 10^{-3} \text{ M}$ , etc., solutions were produced from dilution for the original 1 M KCl solution. The electrical DC potential was supplied by a precision Source/Measure Unit (SMU) (B2902A, Keysight Technologies, Inc., CA, USA) to characterize ion transport through the membrane at various biases. For collecting signals of each electrode parallelly a digital eight channels oscilloscope (PicoScope 4824, Pico Technology, St. Neots, UK) with a sampling rate of  $1 \text{ MS s}^{-1}$  was used. (Details on the electrochemical characterization are provided in Note S1, Supporting Information.)

**Surface Functionalization of PDMS Membrane with PNIPAM Brushes:** First, the surface of freestanding PDMS membrane without embedded electrode with single hole (slit shape) was functionalized with oxygen plasma (35 SCCM  $\text{O}_2$ , 50 W for 30 s), followed by emerging the samples in APTES: ethanol solution (1:2 v/v) for 5 min and carefully dried with nitrogen flow. APTES and ethanol were provided from Sigma-Aldrich Co. LLC., Germany and VWR, Darmstadt, Germany, respectively. Afterward, samples were emerged in ammonia solution 32% (Sigma-Aldrich Co. LLC., Germany) for 3 min and carefully dried with nitrogen flow.<sup>[73]</sup> HOOC-PNIPAM-H polymers were dispersed in MES buffer ( $100 \times 10^{-3} \text{ M}$ , pH 5.5) in 10:1 (w/v) ratio. Then DMTMM 0.05% (w) compared to PNIPAM chains were added to the solution and mixed for 30 min. A droplet of this solution was then added onto the PDMS membrane, on-top of the hole region, and the system was placed in a humid glass sealed chamber (with an exposed volume of water inside) for 12 h. The membranes were subsequently washed with Milli-Q water (two times), then a large droplet of water was placed on the membrane and allowed to stand for 2 h to solubilize any nonconjugated chains, which was subsequently thoroughly washed with Milli-Q (five times) and dried under argon (details on the surface functionalization of PDMS membrane with PNIPAM brushes are provided in Note S6, Supporting Information). The membranes were characterized by contact angle measurements (OCA40 by DataPhysics Instruments GmbH (Filderstadt, Germany)). All droplets were measured by sessile drop experiments as the advancing and receding contact angles at  $23^\circ\text{C}$  with Milli-Q water. The droplet profile was evaluated by the tangent learning method.

**Statistical Analysis:** All qualitative data presented for I-V measurements are results of three measurements. PDMS mechanical properties consist of mean thickness and Young's modulus of PDMS film (presented in Figure S2 and Note S3, Supporting Information), error bars are standard deviations of three different measurements with 95% confidence interval from different samples. Detail description for each data presentation is available in the Supporting Information.

## Supporting Information

Supporting Information is available from the Wiley Online Library or from the author.

## Acknowledgements

The authors acknowledge C. Krien, K. Leger, L. Raith, C. Schmidt, S. Nestler, M. Bauer, A. Mirhajivarzaneh, and R. Engelhard (all Leibniz IFW Dresden) for the deposition of metallic thin films, synthesis of materials, and technical support in the clean room. The authors thank Dr. A. I. Egunov, Z. Dou, F. Akbar, B. Rivkin, E. Eisner (all Leibniz IFW Dresden) for helpful discussions and L. Fietzke and R. Jordan from the Technische Universität Dresden for assistance with GPC. This work is part of the projects that have received funding from the German Research Foundation DFG (Gottfried Wilhelm Leibniz Prize granted in 2018, SCHM 1298/22-1 and KA5051/1-1 and KA5051/3-1), the Leibniz association (Leibniz Transfer Program T62/2019), and the Alexander von Humboldt foundation (Q.A.B.).

Open access funding enabled and organized by Projekt DEAL.

## Conflict of Interest

The authors declare no conflict of interest.

## Data Availability Statement

The data that support the findings of this study are available from the corresponding author upon reasonable request.

## Keywords

elastomeric membranes, ion transport, membranotronics, negative differential resistance, PDMS, PNIPAM

Received: February 4, 2022

Revised: February 28, 2022

Published online: March 9, 2022

- [1] C. Leterrier, *J. Neurosci.* **2018**, *38*, 2135.
- [2] E. R. Kandel, J. H. Schwartz, T. M. Jessell, S. A. Siegelbaum, *Principles of Neural Science*, McGraw-Hill, New York **2000**.
- [3] C. E. Holt, K. C. Martin, E. M. Schuman, *Nat. Struct. Mol. Biol.* **2019**, *26*, 557.
- [4] J. Zhu, T. Zhang, Y. Yang, R. Huang, *Appl. Phys. Rev.* **2020**, *7*, 011312.
- [5] Z. Wang, M. Rao, J. W. Han, J. Zhang, P. Lin, Y. Li, C. Li, W. Song, S. Asapu, R. Midya, Y. Zhao, H. Jiang, J. H. Yoon, N. K. Upadhyay, S. Joshi, M. Hu, J. P. Strachan, M. Barnell, Q. Wu, H. Wu, Q. Qiu, R. S. Williams, Q. Xia, J. J. Yang, *Nat. Commun.* **2018**, *9*, 1.
- [6] S. Renaud, J. Tomas, Y. Bornat, A. Daouzli, S. Saïghi, *Proc. – IEEE Int. Symp. Circuits Syst.* **2007**, 3355.
- [7] C. Wan, G. Chen, Y. Fu, M. Wang, N. Matsuhisa, S. Pan, L. Pan, H. Yang, Q. Wan, L. Zhu, X. Chen, *Adv. Mater.* **2018**, *30*, 1801291.
- [8] X. Hou, W. Guo, L. Jiang, *Chem. Soc. Rev.* **2011**, *40*, 2385.
- [9] I. Vlassiuk, S. Smirnov, Z. Siwy, *Nano Lett.* **2008**, *8*, 1978.
- [10] P. Y. Apel, Y. E. Korchev, Z. Siwy, R. Spohr, M. Yoshida, *Nucl. Instrum. Methods Phys. Res., Sect. B* **2001**, *184*, 337.
- [11] J. Cervera, B. Schiedt, R. Neumann, S. Mafá, P. Ramírez, *J. Chem. Phys.* **2006**, *124*, 104706.
- [12] X. He, K. Zhang, T. Li, Y. Jiang, P. Yu, L. Mao, *J. Am. Chem. Soc.* **2017**, *139*, 1396.
- [13] P. Ramirez, J. J. Perez-Grau, J. Cervera, S. Nasir, M. Ali, W. Ensinger, S. Mafe, *Appl. Phys. Lett.* **2021**, *118*, 181903.
- [14] H. Yang, G. Qing, *Chem. Phys. Rev.* **2021**, *2*, 021306.
- [15] M. R. Powell, M. Sullivan, I. Vlassiuk, D. Constantin, O. Sudre, C. C. Martens, R. S. Eisenberg, Z. S. Siwy, *Nat. Nanotechnol.* **2008**, *3*, 51.
- [16] B. Hyland, Z. S. Siwy, C. C. Martens, *J. Phys. Chem. Lett.* **2015**, *6*, 1800.
- [17] Y. Li, G. Du, J. Zhao, J. Guo, R. Wu, W. Liu, G. Mao, C. Shen, *Chem-NanoMat* **2020**, *6*, 1075.
- [18] E. B. Kalman, O. Sudre, I. Vlassiuk, Z. S. Siwy, *Anal. Bioanal. Chem.* **2009**, *394*, 413.
- [19] Y. Tian, L. Wen, X. Hou, G. Hou, L. Jiang, *ChemPhysChem* **2012**, *13*, 2455.
- [20] E. Perozo, D. M. Cortes, P. Sompornpisut, A. Kloda, B. Martinac, *Nature* **2002**, *418*, 942.
- [21] M. Abdelsayed, S. Sokolov, *Channels* **2013**, *7*, 146.
- [22] X. Hou, Y. Hou, *Science* **2021**, *373*, 628.
- [23] W. Guo, Y. Tian, L. Jiang, *Acc. Chem. Res.* **2013**, *46*, 2834.
- [24] Z. Zhang, L. Wen, L. Jiang, *Chem. Soc. Rev.* **2018**, *47*, 322.
- [25] K. Zhan, Z. Li, J. Chen, Y. Hou, J. Zhang, R. Sun, Z. Bu, L. Wang, M. Wang, X. Chen, X. Hou, *Nano Today* **2020**, *33*, 100868.
- [26] T. F. Otero, J. G. Martinez, J. Arias-Pardilla, *Electrochim. Acta* **2012**, *84*, 112.
- [27] V. K. Sangwan, M. C. Hersam, *Nat. Nanotechnol.* **2020**, *15*, 517.
- [28] P. Janson, E. O. Gabrielsson, K. J. Lee, M. Berggren, D. T. Simon, *Adv. Mater. Technol.* **2019**, *4*, 1800494.
- [29] C. H. Yang, B. Chen, J. J. Lu, J. H. Yang, J. Zhou, Y. M. Chen, Z. Suo, *Extreme Mech. Lett.* **2015**, *3*, 59.
- [30] H. Chun, T. D. Chung, *Annu. Rev. Anal. Chem.* **2015**, *8*, 441.
- [31] B. Lovreček, A. Despić, J. O. M. Bockris, *J. Phys. Chem.* **1959**, *63*, 750.
- [32] W. Chen, Q. Wang, J. Chen, Q. Zhang, X. Zhao, Y. Qian, C. Zhu, L. Yang, Y. Zhao, X. Y. Kong, B. Lu, L. Jiang, L. Wen, *Nano Lett.* **2020**, *20*, 5705.
- [33] A. Studer, X. Han, F. K. Winkler, L. X. Tiefenauer, *Colloids Surf., B* **2009**, *73*, 325.
- [34] D. T. Simon, K. C. Larsson, D. Nilsson, G. Burström, D. Galter, M. Berggren, A. Richter-Dahlfors, *Biosens. Bioelectron.* **2015**, *71*, 359.
- [35] P. Janson, E. O. Gabrielsson, K. J. Lee, M. Berggren, D. T. Simon, *Adv. Mater. Technol.* **2019**, *4*, 1800494.
- [36] D. Huh, K. L. Mills, X. Zhu, M. A. Burns, M. D. Thouless, S. Takayama, *Nat. Mater.* **2007**, *6*, 424.
- [37] M. Wang, Y. Hou, L. Yu, X. Hou, *Nano Lett.* **2020**, *20*, 6937.
- [38] M. Wang, H. Meng, D. Wang, Y. Yin, P. Stroeve, Y. Zhang, Z. Sheng, B. Chen, K. Zhan, X. Hou, *Adv. Mater.* **2019**, *31*, 1805130.
- [39] A. L. Hodgkin, A. F. Huxley, *J. Physiol.* **1945**, *104*, 176.
- [40] I. Tasaki, K. Kusano, P. M. Byrne, *Biophys. J.* **1989**, *55*, 1033.
- [41] A. Gonzalez-Perez, L. D. Mosgaard, R. Budvytyte, E. Villagran-Vargas, A. D. Jackson, T. Heimburg, *Biophys. Chem.* **2016**, *216*, 51.
- [42] T. Heimburg, A. D. Jackson, *Proc. Natl. Acad. Sci. USA* **2005**, *102*, 9790.
- [43] S. S. L. Andersen, A. D. Jackson, T. Heimburg, *Prog. Neurobiol.* **2009**, *88*, 104.
- [44] H. Le-The, M. Tibbe, J. Loessberg-Zahl, M. Palma Do Carmo, M. Van Der Helm, J. Boemer, A. Van Den Berg, A. Leferink, L. Segerink, J. Eijkel, *Nanoscale* **2018**, *10*, 7711.
- [45] S. J. A. Koh, C. Keplinger, T. Li, S. Bauer, Z. Suo, *IEEE/ASME Trans. Mechatron.* **2011**, *16*, 33.
- [46] Q. A. Besford, H. Yong, H. Merlitz, A. J. Christofferson, J. Sommer, P. Uhlmann, A. Fery, *Angew. Chem.* **2021**, *133*, 16736.
- [47] J. L. Hutter, J. Bechhoefer, *Rev. Sci. Instrum.* **1993**, *64*, 1868.
- [48] B. Liu, J. Fu, *J. Micromech. Microeng.* **2015**, *25*, 065006.
- [49] D. Qi, K. Zhang, G. Tian, B. Jiang, Y. Huang, *Adv. Mater.* **2021**, *33*, 2003155.
- [50] S. Wagner, S. Bauer, *MRS Bull.* **2012**, *37*, 207.
- [51] D. Karnaushenko, N. Münzenrieder, D. D. Karnaushenko, B. Koch, A. K. Meyer, S. Baunack, L. Petti, G. Tröster, D. Makarov, O. G. Schmidt, *Adv. Mater.* **2015**, *27*, 6797.
- [52] D. Karnaushenko, D. D. Karnaushenko, D. Makarov, S. Baunack, R. Schäfer, O. G. Schmidt, *Adv. Mater.* **2015**, *27*, 6582.
- [53] Z. S. Siwy, *Adv. Funct. Mater.* **2006**, *16*, 735.
- [54] L. Cao, W. Guo, Y. Wang, L. Jiang, *Langmuir* **2012**, *28*, 2194.
- [55] L. J. Cheng, L. J. Guo, *Nano Lett.* **2007**, *7*, 3165.
- [56] W. Guo, L. Cao, J. Xia, F. Q. Nie, M. Wen, J. Xue, Y. Song, D. Zhu, Y. Wang, L. Jiang, *Adv. Funct. Mater.* **2010**, *20*, 1339.
- [57] H. C. Yeh, C. C. Chang, R. J. Yang, *RSC Adv.* **2014**, *4*, 2705.
- [58] M. Lepoittevin, T. Ma, M. Bechelany, J. M. Janot, S. Balme, *Adv. Colloid Interface Sci.* **2017**, *250*, 195.
- [59] B. Yameen, M. Ali, R. Neumann, W. Ensinger, W. Knoll, O. Azzaroni, *Small* **2009**, *5*, 1287.
- [60] A. Halperin, M. Kröger, F. M. Winnik, *Angew. Chem., Int. Ed.* **2015**, *54*, 15342.
- [61] Y. Xiang, B. Li, Y. Zhang, S. Ma, B. Li, H. Gao, B. Yu, J. Li, F. Zhou, *ACS Appl. Mater. Interfaces* **2019**, *11*, 36073.
- [62] H. Nagase, K. Okano, T. Kanazawa, *Nano-Struct. Nano-Objects* **2018**, *16*, 9.

- [63] D. Kuckling, H. J. P. Adler, K. F. Arndt, L. Ling, W. D. Habicher, *Macromol. Chem. Phys.* **2000**, 201, 273.
- [64] S. Rauch, K. J. Eichhorn, D. Kuckling, M. Stamm, P. Uhlmann, *Adv. Funct. Mater.* **2013**, 23, 5675.
- [65] H. Yong, B. Molcrette, M. Sperling, F. Montel, J. U. Sommer, *Macromolecules* **2021**, 54, 4432.
- [66] C. Zhou, S. Bette, U. Schnakenberg, *Adv. Mater.* **2015**, 27, 6664.
- [67] A. El Hady, B. B. Machta, *Nat. Commun.* **2015**, 6, 6697.
- [68] D. L. Sekulic, M. V. Sataric, M. B. Zivanov, J. S. Bajic, *Elektron. Elektrotech.* **2012**, 5, 53.
- [69] Y. Klofaï, B. Z. Essimbi, D. Jöger, *Phys. Scr.* **2015**, 90, 025002.
- [70] R. Landauer, *IBM J. Res. Dev.* **2010**, 4, 391.
- [71] A. J. Fairbanks, A. M. Darr, A. L. Garner, *IEEE Access* **2020**, 8, 148606.
- [72] R. Rodwell, M. J. Allen, S. T. Yu, R. Y. Case, M. G. Bhattacharya, U. Reddy, M. Carman, E. Kamegawa, M. Konishi, Y. Pusl, J. Pullela, *Proc. IEEE* **1994**, 82, 1035.
- [73] J. H. L. Beal, A. Bubendorfer, T. Kemmitt, I. Hoek, W. M. Arnold, *Biomicrofluidics* **2012**, 6, 036503.
- [74] M. Liu, J. Sun, Y. Sun, C. Bock, Q. Chen, *J. Micromech. Microeng.* **2009**, 19, 17.